Aeroacoustic wave equation based on Pierce's operator applied to the sound generated by a mixing layer

Stefan Schoder*, Manfred Kaltenbacher[†]

Institute of Fundamentals and Theory in Electrical Engineering, Technische Universität Graz, Inffeldgasse 18, 8010 Graz, Austria

Étienne Spieser[‡], Hugo Vincent[§], Christophe Bogey[¶], and Christophe Bailly[‖]

Univ Lyon, École Centrale de Lyon, CNRS, Univ Claude Bernard Lyon 1, INSA Lyon, LMFA, UMR5509, 69130, Écully, France

For the first time, this paper presents the sound prediction capabilities of an aeroacoustic wave equation based on Pierce's operator (AWE-PO). The wave equation is applied to a two-dimensional mixing layer, providing a solution which is compared with the far-field acoustics of a direct numerical simulation. In contrast to a direct numerical simulation, the computed Lighthill's wave equation and the AWE-PO rely on a hybrid workflow to predict the generated sound. Special attention is put on the visualization and interpretation of the right-hand side of both equations. Finally, the results of the acoustic far-field pressure are compared. It is shown that the radiated sound field's directivity, propagation, and convection effects are captured well for both wave equations. The error of the acoustic intensity compared with the direct numerical simulation is less than 2 dB for Lighthill's equation and AWE-PO. This error is comparable with the errors reported for Lighthill's equation in previous studies. To conclude, the presented wave equation reasonably predicts mixing layer sound, and the acoustic far-field pressure results are in good agreement with the DNS.

I. Introduction

In the modern world, sustainable research and development involve accurate modeling of acoustic emissions. A detailed understanding of sound, the sources of sound, and the energy transformation to acoustic emissions are essential. Starting in 1952, Lighthill [1] looked at the detailed process of the conversion of flow energy to acoustic energy. The exact reformulation of the conservation equations of fluid dynamics into a wave equation leads to a balancing right-hand side (so-called sources). These (sound) sources are responsible for sound generation, attenuation, convection, refraction, and non-linear effects. Ribner [2] linearized the inhomogeneous term of Lighthill's wave equation around the mean flow, which leads to a distinction between shear-noise and self-noise contributions of the energy conversion process. Regarding this differentiation, a right-hand-side term for Pierce's wave operator was introduced in [3] aiming for a new distinction between sources of sound and flow convection effects. It accounts reasonably well for acoustic propagation [4].

In the present work, the hybrid aeroacoustic workflows [5] of Lighthill's equation and the aeroacoustic wave equation based on Pierce's operator (AWE-PO) are implemented. The implementations of the hybrid aeroacoustic workflows are applied to a two-dimensional mixing layer and validated. Therefore, the results are compared with the exact acoustic far-field propagation of a two-dimensional (2D) solution of the conservation equations of fluid dynamics (DNS). During the discussion of the results, special attention is put on the visualization and interpretation of the right-hand side of Lighthill's wave equation and AWE-PO.

The paper is organized as follows. In section II, we will describe the fundamentals of Lighthill's wave equation and the AWE-PO. Section III presents the numerical methods and the hybrid workflow. In section IV, we briefly illustrate

---

*Assistant Professor, Institute of Fundamentals and Theory in Electrical Engineering, Graz, and Visiting Scholar at Fluid Mechanics and Acoustics Laboratory (LMFA), Écully, AIAA Member

[†]Full Professor, Institute of Fundamentals and Theory in Electrical Engineering, Graz, and AIAA Member Senior.

[‡]Postdoctoral Fellow, Fluid Mechanics and Acoustics Laboratory (LMFA), Écully.

[§]Doctoral Candidate, Fluid Mechanics and Acoustics Laboratory (LMFA), Écully.

[¶]Full Professor, Fluid Mechanics and Acoustics Laboratory (LMFA), Écully, and AIAA Member Senior.

[‖]Full Professor, Fluid Mechanics and Acoustics Laboratory (LMFA), Écully, and AIAA Member Senior.

the application of a 2D mixing layer, which is used as validation. The results of the application are summarized in section V and concluded after that in section VI.

II. Theory

The conversion of flow energy to acoustic energy is inherently coupled with the conservation equations of fluid dynamics. This inherent coupling makes a precise investigation of the energy transformation cumbersome. However, all nonlinear coupling effects of the flow and the aeroacoustic sound generation are included.

The first theory that looked detailed into the conversion of flow energy into far-field sound emissions was Lighthill's theory [1]. Lighthill started to quantify the proportion of flow energy converted into sound by reformulating the conservation equations. In doing so, a nonlinear right-hand side term was obtained, which can be simplified for dominant vortical sound sources [6] (e.g., for an isothermal subsonic mixing layer [7, 8]). The Lighthill wave equation reads as

$$\left(\frac{1}{c_0^2} \frac{\partial^2}{\partial t^2} - \nabla \cdot \nabla \right) \left(c_0^2 \rho' \right) = \nabla \cdot \nabla \cdot (\rho \, \boldsymbol{u} \otimes \boldsymbol{u}) \ . \tag{1}$$

where $\rho' = (\rho - \rho_0)$ is the fluctuating density, defined as a perturbation on the mean density ρ_0, c_0 is the isentropic ambient speed of sound, and $\boldsymbol{u}$ is the fluid velocity. Over the years, many authors reported prediction methods for flow-induced sound [5]. For instance, Ribner linearized the right-hand side around the mean flow $\boldsymbol{u}_0$ to emphasize the contribution of the fluctuating flow $\boldsymbol{u}'$ to the sound generation. This linearization leads to a fundamental distinction between shear-noise $2\rho_0(\nabla \boldsymbol{u}_0) : (\nabla \boldsymbol{u}')$ and self-noise $\rho_0 \nabla \cdot \nabla \cdot (\boldsymbol{u}' \otimes \boldsymbol{u}')$ contributions of the energy conversion process [2, 9].

An alternative acoustic wave equation (AWE-PO) can be derived, ending up at Pierce's wave operator, AWE-PO, that considers an acoustic potential of the fluctuating momentum ϕ as the dependent variable [3]. Now, ϕ is defined by Helmholtz decomposition of the fluctuating momentum as, $\rho_0 \boldsymbol{u}' = \nabla \times \boldsymbol{B} + \nabla \phi$, with $\boldsymbol{B}$ being the vortical momentum vector potential. Neglecting the vortical interaction inside the wave operator leads to a second-order convective wave operator [10]

$$\frac{D^2 \phi}{Dt^2} - \nabla \cdot (c_0^2 \nabla \phi) = \frac{DS_{\mathrm{m}}}{Dt} \tag{2}$$

where D/Dt denotes the total derivative concerning the mean flow $\boldsymbol{u}_0$, S_{m} the source potential, and the equation's source term obeys the Poisson equation (Laplace-filtering)

$$\nabla \cdot \nabla S_{\mathrm{m}} = \Delta S_{\mathrm{m}} = \nabla \cdot \nabla \cdot (\rho_0 \boldsymbol{u}' \otimes \boldsymbol{u}') \ . \tag{3}$$

In this sense, the self-noise source term is filtered to obtain the radiating source potential S_{m}. This filtering process isolates the radiating sound sources that force the wave equation. First investigations of the equation show that it accounts reasonably well for the acoustic propagation [4]. This computation will support previous findings and compare the newly derived AWE-PO to Lighthill's equation and the DNS as a benchmark.

III. Methods

The acoustic field is computed with a hybrid aeroacoustic workflow [5] in three steps. Firstly, the flow field is obtained using finite differences to discretize the conservation equations. Secondly, the right-hand sides of the Lighthill's wave equations and AWE-PO are computed. Finally and depending on the wave equation used, the sound propagation is simulated respectively. The hybrid approach is beneficial since the transformed energy from flow to acoustics can be quantified accordingly.

A. Step I: Flow simulation

The DNS of the mixing layer is carried out using an in-house solver to model the two-dimensional compressible Navier-Stokes equations in Cartesian coordinate (x, y), based on low-dissipation and low-dispersion explicit schemes. Fourth-order eleven-point centered finite differences are used for spatial discretization, allowing accuracy down to four points per wavelength, and a second-order six-stage Runge-Kutta algorithm is implemented for time integration [11]. A sixth-order eleven-point centered filter [12] is applied explicitly to the flow variables every time step to remove grid-to-grid oscillations without affecting the waves computed. Non-centered finite differences and filters are also used

near the grid boundaries [13]. At the boundaries, the radiation conditions of Tam & Dong [14] are applied, with the addition at the outflow of a sponge zone combining grid stretching and Laplacian filtering [15], to avoid significant acoustic reflections.

B. Step II: Source term computation

Regarding best practice for hybrid aeroacoustics source computations for finite element method [16, 17], the right-hand sided of (1) and (2) were computed on the flow lattice and conservatively integrated to the finite element mesh [18, 19]. The conservative integration by the cell-centered method was benchmarked by the superior cut-volume cell method with a negligible error of 0.1%. Consequently, the computationally more efficient cell-centered integration was used for this study.

1. Lighthill's wave equation

The sources of sound using Lighthill's wave equation (1) are computed from the flow field using the finite difference method. To avoid the drift of the acoustic pressure (as noticed in [20]), the mean part of the source term of Lighthill's equation is eliminated [21].

2. Aeroacoustic wave equation based on Pierce's wave operator (AWE-PO)

The Laplace-filtering equation (3) was solved using the openCFS [22] method *acousticSplitPDE* with the option *scalar* to computing the scalar part of the Helmholtz decomposition [23–25]. The computational domain coincides with the 2D flow domain and uses the finite difference points as finite element nodes. Linear quadrilateral Lagrangian finite elements are used. An infinite mapping layer surrounds this domain and uses the 2D free-field characteristics to account for the elliptic free-field [26]. Each time step can be filtered individually, decreasing the duration of this workflow step significantly with parallel processes. Based on the Laplace-filtered potential S_m, the source for AWE-PO (2) is computed accordingly.

C. Step III: Acoustic simulation

Lighthill's equation (1) and AWE-PO (2) are solved using the openCFS [22] method *acousticPDE*. The computational domain has the dimensions of the flow domain. A perfectly matched layer (PML) with an inverse damping function region surrounds the mesh [27] to reduce boundary reflections. The mean flow velocity $\boldsymbol{u}_0$ is prescribed for the AWE-PO to model the convective wave operator. The AWE-PO is solved with a stable convective wave formulation [28]. Both Lighthill's equation and AWE-PO are approximated using uniform quadrilateral Lagrangian finite elements of the first order. A systematic mesh study was performed to guarantee a sufficient accurate resolution. The given source data fixes the time step size, and the acoustic field was initialized homogeneously. The dispersion-controlled Hilbert-Taylor-Hughes scheme performs time stepping.

IV. Application

As in previous studies [29–37], a two-dimensional isothermal mixing layer is considered with the aim of assessing the validity of acoustic wave equations. The flow configuration is similar to those simulated by Colonius *et al.* [38] and Bogey *et al.* [21]. For illustration, a schematic view of the configuration is shown in figure 1. The mixing layer is centered at $y = 0$. The velocity at the inflow boundary condition is given by the hyperbolic-tangent profile

$$u(y) = \frac{U_1 + U_2}{2} - \frac{U_2 - U_1}{2} \tanh\left(\frac{2y}{\delta_\omega}\right) \tag{4}$$

where $U_1 = 0.3c_0$ and $U_2 = 0.6c_0$ are the velocities of the slow and rapid flows, respectively. δ_ω is the vorticity thickness at the upstream boundary which provides a Reynolds number of $Re_\omega = \delta_\omega(U_2 - U_1)/\nu = 2000$, where ν is the kinematic molecular viscosity.

For the DNS, a domain of dimension $L_x = 600\delta_\omega$ and $L_y = 400\delta_\omega$ is used. This domain is discretized by a non-uniform structured grid. In the transverse direction, the mesh spacing is equal to $\Delta y_0 = 0.1\delta_\omega$ at $y = 0$. On both sides of the mixing layer, this mesh spacing is stretched with a rate of 4% until it reaches $\Delta y \approx 2.3\delta_\omega$ at $y \approx \pm 55\delta_\omega$. In the axial direction, the mesh spacing is equal to $\Delta x_0 = 0.2\delta_\omega$ from $x = 0$ to $x = 250\delta_\omega$. Farther downstream, a sponge zone is implemented, and the mesh spacing is stretched at a rate of 4%. In this sponge zone, the variables are
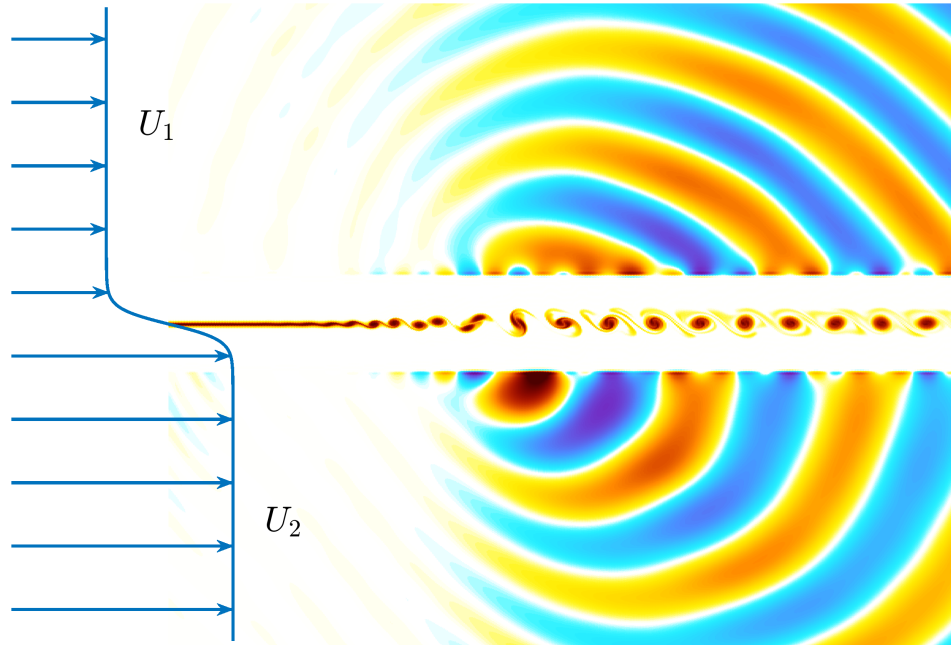
Fig. 1   Schematic view of the mixing layer. Instantaneous vorticity and fluctuating pressure fields are represented at the center and periphery of the shear zone, respectively. Only a part of the domain is shown.

filtered using a Laplacian filter with an intensity growing linearly from zero at $x = 250\delta_\omega$ up to 0.2 at $x = 350\delta_\omega$. For $x > 350\delta_\omega$, the intensity is constant and equal to 0.2. The time step size, based on the minimum mesh spacing in the transverse direction and the speed of sound in the ambient medium, is given by $\Delta t = \Delta y_0 / c_0$. The mixing layer is excited at its fundamental frequency f, given by the Strouhal number $St_\omega = 2f\delta_\omega/(U_2 + U_1) = 0.141$ [39], and at the first subharmonic $f/2$. This excitation allows the formation of vortices at a fixed position $x \approx 70\delta_\omega$ and also the occurrence of vortex pairings at $x \approx 110\delta_\omega$. In figure 1, these vortices and their periodically pairings (vortex pairing period $T_p = 2/f$) can be observed at the center of the shear zone. Each vortex pairing period is discretized by $\Delta t/T_p = 1/315$, and after $500T_p$ pre-computation the DNS data is stored at every third time step for the computation of the right-hand side of (1) and (3). In total, a duration of $50T_p$ are computed and exported for this investigation. The vortex pairings generate acoustic waves at a frequency $f/2$ in the acoustic field, as seen in the figure 1. Regarding figure 1, it can be noted that they constitute the only sound sources inside the mixing layer.

For the acoustic computation, the domain size is the same as for the DNS simulation. The mesh uses a uniform discretization of $\Delta x \approx 0.17\delta_\omega$ and $\Delta y \approx 0.35\delta_\omega$. The PML uses the same discretization with four layers of elements towards the free-field direction. The grid resolution and the PML layer amount were studied to ensure an accurate resolution of the respective equations.

V. Results

Inside this section, we will discuss the results of Lighthill's equation (1) and the AWE-PO (2). These results are then compared systematically with the far-field solution of the DNS. Firstly, we will illustrate sequences of the source terms and compare them accordingly. Secondly, the acoustic propagation results are analyzed in detail by snapshots of the pressure field and the radiation characteristics of the acoustic intensity centered around the vortex pairing location.

A. Visualization of sound sources

The sound sources are plotted at three frames over one vortex pairing period T_p, to analyze the temporal evolution of the individual sources of the respective equations (reported in section III). All source illustrations are given in a rectangular cutout of $-15 < y/\delta_\omega < 15$, where the instability waves grow and consequently the most dominant source terms occur [7, 33]. Figure 2 visualizes the sources of Lighthill's equation (1) and shows the merging of two consecutive

4

vortices at the time $t \approx t_0 + T_\text{p}/3$ and location $x/\delta_\omega \approx 110$. Lighthill's equation's source characteristics were previously investigated in [7, 8, 20, 21, 40] and the authors obtained similar source distributions. Between the moving vortices (red dots), steady source regions of relatively high magnitude are visible. Ribner [2] concluded that this component (products of the mean flow and fluctuating flow) of the overall source term does not radiate but accounts for convection and refraction effects. This motivates further manipulations to isolate the source term from convection and refraction effects while maintaining the energy transformation of the sound generation process.
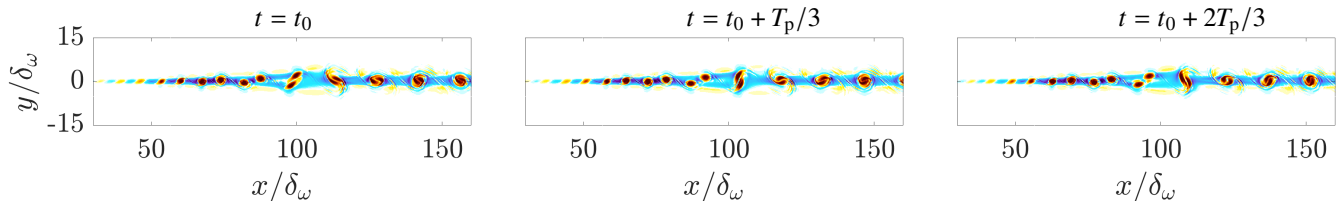
Fig. 2   Lighthill's right-hand-side term of equation (1)**, using a color scale minimum and maximum of** $\pm 3 \cdot 10^{10}\,{}^{\text{kg}}\!/_{(\text{m}^3\text{s}^2)}$**, respectively.**

In doing so, the distinction between self-noise and shear-noise emerged [2]. The shear-noise part of the Lighthill right-hand-side for compressible flows reads as

$$\nabla \cdot \nabla \cdot (\rho_0 \left(\boldsymbol{u}_0 \otimes \boldsymbol{u}' + \boldsymbol{u}' \otimes \boldsymbol{u}_0 \right)) \ . \tag{5}$$

Figure 3 illustrates the temporal evolution of the shear-noise source term over one vortex merging period T_p. The transitions of the source structures depict the interactions of the mean flow with the fluctuating velocity and account for regions of high source values between the moving vortices in figure 2.
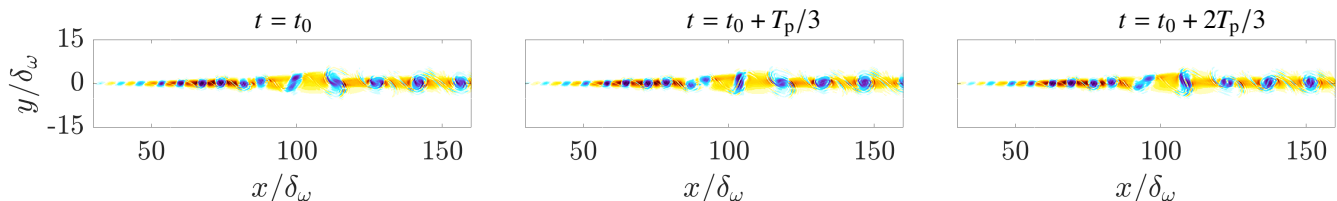

Fig. 3   Shear-noise part of Lighthill's right-hand-side term (5)**, using a color scale minimum and maximum of** $\pm 3 \cdot 10^{10}\,{}^{\text{kg}}\!/_{(\text{m}^3\text{s}^2)}$**, respectively.**

Figure 4 visualizes the self-noise part defined by equation (3) and shows again the merging of two consecutive vortices at time $t \approx t_0 + T_\text{p}/3$ and location $x/\delta_\omega \approx 110$. Compared to Lighthill's source term, the source strength is concentrated at the location of the merging vortices, where sound waves are produced. The source term (3) has a strongly reduced source content between the moving vortices with respect to Lighthill's source term in figure 2. Still,
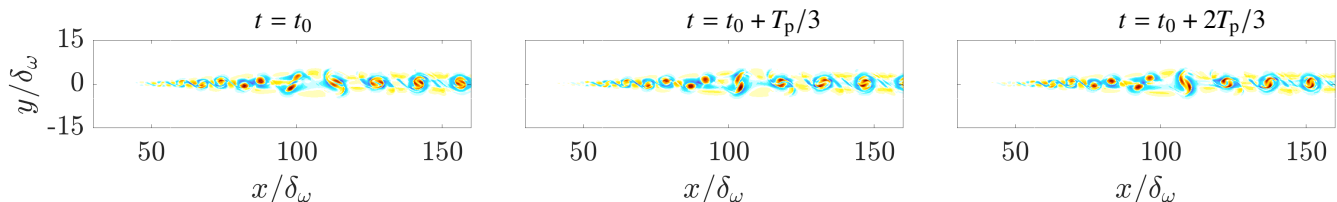

Fig. 4   Self-noise part of Lighthill's right-hand-side term, which is the source of equation (3)**, using a color scale minimum and maximum of** $\pm 3 \cdot 10^{10}\,{}^{\text{kg}}\!/_{(\text{m}^3\text{s}^2)}$**, respectively.**

the shape of the vortical sound sources significantly deviates from the theoretical quadrupolar vortex sound source shape. Overall, the gradients of the source term at the pairing location and pairing time are pronounced.

Figure 5 shows the material derivative of the Laplace filtered source potential S_m, defining the source of AWE-PO (2). The moving vortices look like stable moving quadrupoles that encounter some strong disturbance at vortex pairing. At this location, the vortices rotate and merge. Furthermore, the amplitude of the sources is much weaker than Lighthill's right-hand side (see figure 2), the shear-noise term (see figure 3), and the self-noise term (see figure 4). We observe an effect that the time derivative and convective derivative of the scalar source potential S_m (associated with a vortex) partially compensate for each other. This compensation results in an overall source amplitude of about one order of magnitude smaller than the two individual additive parts (time derivative and convective derivative) of the material derivative. This compensation effect will be discussed in detail in appendix VI.
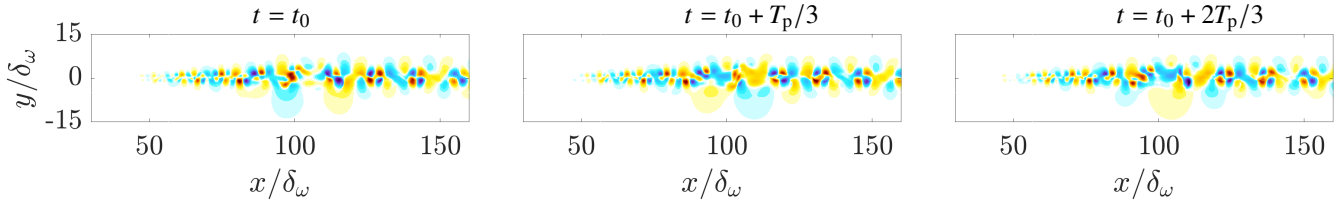

Fig. 5 **Visualization of the right-hand-side of AWE-PO** (2)**, using a color scale minimum and maximum of** $\pm 3 \cdot 10^9$ kg/(m³s²)**, respectively. Comparability to the other source plots is achieved by including a relevant pre-factor** $1/(c_0^2 \Delta t)$ **to obtain the solution variable** p' **after solving AWE-PO for the scalar potential** ϕ**.**

The source terms, illustrated by the figure 2 - 5, do differ in shape and magnitude regarding their definition. The amplitude of Lighthill's source is significant in the whole extent of the shear layer, as observed by Colonius *et al.* [38] in their study of Lilley's acoustic analogy. This high magnitude can be explained by the definition of the Lamb vector (the cross product of the vorticity and the velocity) being one major part of the Lighthill's source and having a high value in sheared fluid zones. However, only the distortion of vortices generates sound [41]. This fact also holds for the AWE-PO. These distortions coincide here with the merging of the vortices. Interestingly, the sources of AWE-PO are quadrupolar, known from theoretical considerations of vortex sound. Although this is obvious, this is an interesting fact that could provide more evidence on the energy transformation process from the vortical flow to acoustics.

B. Acoustic solution

After discussing the source term, the far-field radiation of the simulations performed is studied. The pressure fluctuations p' obtained are compared against each other. The fluctuating pressure of Lighthill's equation is defined by $p' = c_0^2 \rho'$ [8], whereas the fluctuating pressure of AWE-PO is calculated by $p' = D\phi/Dt$. Within this section, the instantaneous fluctuating pressure fields p', and the acoustic intensity being proportional to the root means square of the fluctuating pressure p_{rms} are compared. The acoustic intensity for spherical waves

$$L_I = 10 \log \frac{I}{I_0} , \tag{6}$$

where $I = p_{rms}^2/(\rho_0 c_0)$ and $I_0 = 10^{-12}$ W/m² is used.

Figure 6 illustrates the fluctuating pressure fields p' obtained by the DNS, Lighthill's wave equation, and AWE-PO. The agreement of the three fields is reasonably good. Nevertheless, minor deviations occur in a few areas of the results. Overall, the results agree well above the mixing layer. Upside and downstream of the mixing layer, the results of Lighthill's equation slightly deviate (upstream up to 2 dB and downstream with a maximum of about 0.5 dB) from the DNS in an approximate 30 degree cones. The upstream deviation is larger for the results of the AWE-PO, which has an extinction line at 12 degrees. A similar extinction line was found in [7] and associated with insufficient integration over the source region regarding the *x*-direction. The insufficient integration over the source region was examined but not found to be the case for AWE-PO. Furthermore, the fluctuating pressure results of AWE-PO contain weak reflections due to an insufficient PML regarding the convective wave operator.

On the lower side, the radiation characteristics and the convective effects for this $M = 0.6$ region are captured well for all computational methods. The solution from Lighthill's equation and AWE-PO have some grid oscillations in the
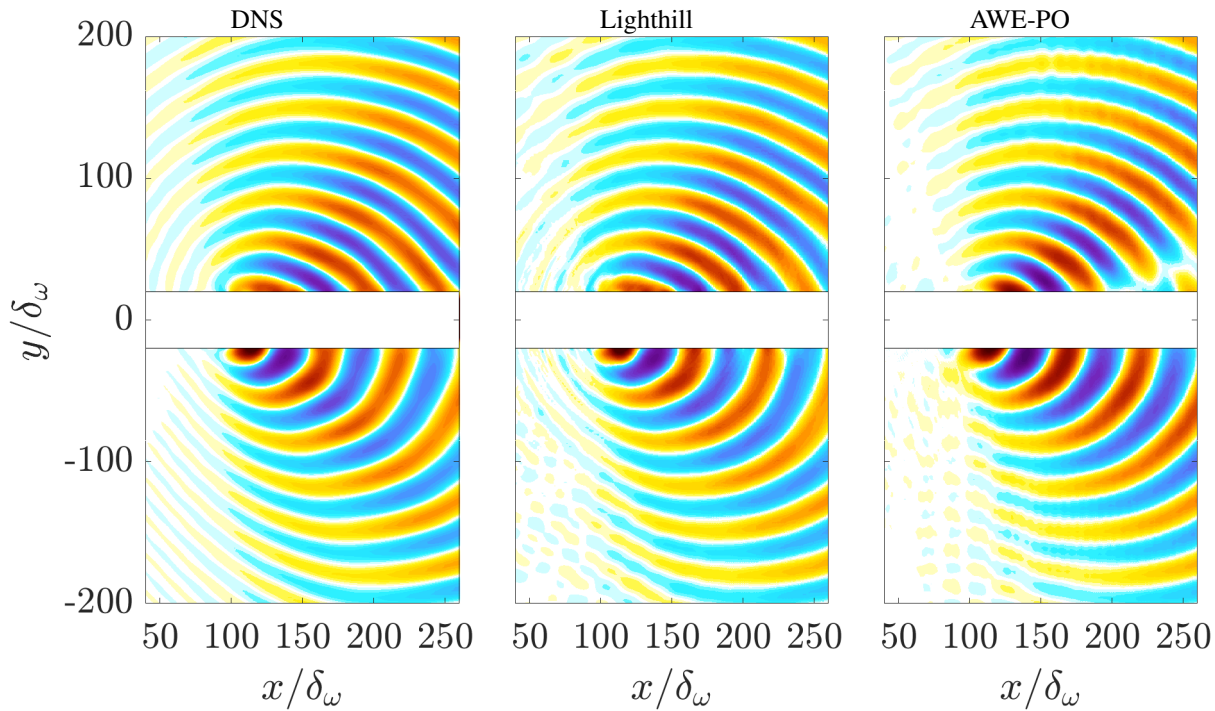
6

Fig. 6   Far-field radiation characteristics of the fluctuating pressure fields p', on the left the result of the DNS, in the middle the results of Lighthill's equation (1)**, and on the right the result of AWE-PO** (5)**. The source region in the middle of each plot is shaded white. The plots use a color scale minimum and maximum value of** ± 15 Pa**.**

upstream direction. A conducted mesh study showed that this is not due to insufficient mesh refinement. For Lighthill's theory, the oscillations are most likely due to the sharp source truncation towards the upstream PML. For the AWE-PO, this is due to PML reflections. The more pronounced oscillations on the lower side are another strong indicator that the PML's accuracy decreases with increasing Mach number.

As a next step, we will look into more details on the self-noise and shear-noise contributions of Lighthill's equation (1). Figure 7 shows the different contributions to the fluctuating pressure fields p', regarding self-noise and shear-noise and the superposition of the individual far-field pressure fields. Interestingly, both parts (self-noise and shear-noise) strongly overpredict the sound field but individually compensate each other in the superposed fluctuating pressure field p', to accurately predict emissions and convection effects. This effect can be interpreted from the results by Freund [9]. In [9], the power generated by the individual shear-noise and self-noise term is larger than the power generated by the overall Lighthill source term. This inequality reveals the compensation effects of the source terms in the radiated acoustics accounting for refraction and convection. Interestingly, the assumption that first-order contributions should be moved to the wave operator [42, 43] cannot be observed by these evaluations directly. On the other hand, the wavefronts of the shear-noise part are distorted oddly to compensate for these convection effects. To conclude, a more detailed investigation regarding the convection effects could shed light on this topic.

Figure 8 compares the directivity computed by considering an origin of the sound emission at the location of the vortex pairing $x/\delta_\omega \approx 110$ and $y/\delta_\omega = 0$. Based on this origin, two arc sections above and below the mixing layer are used to calculate the acoustic intensity. The evaluation arcs exclude the results inside the mixing layer since they are not comparable throughout the different methods (angles upstream between ± 10 degrees are not included). Upstream, the angles larger than ± 150 degrees, are not included in the evaluation since the evaluation points would be outside
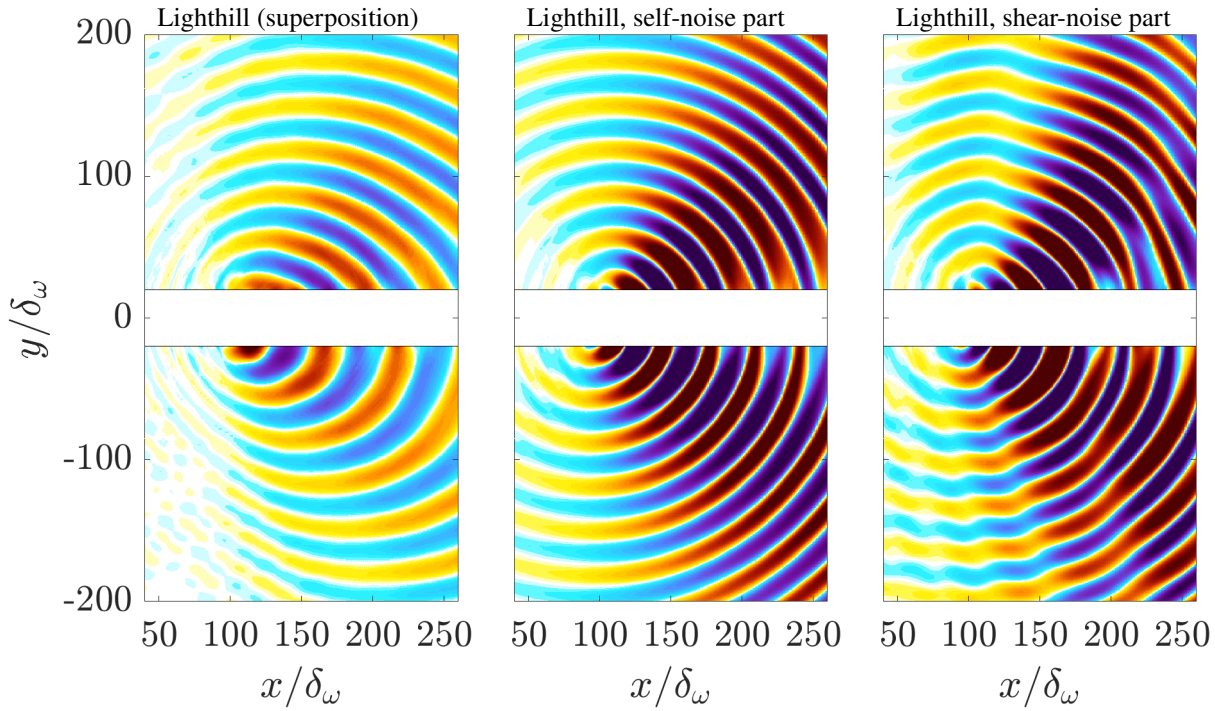
Fig. 7 Far-field radiation characteristics of the fluctuating pressure fields p'**, on the left the result of the Lighthill's equation** (1) **regarding the superposition of the self-noise and the shear-noise result, in the middle the results of the self-noise contribution, and on the right the result of shear-noise contribution. The source region in the middle of each plot is shaded white. The plots use a color scale minimum and maximum value of** $\pm 15\,\mathrm{Pa}$**.**

the computational domain. Overall, the results agree well. For angles close to ± 150 degrees, the results of Lighthill's equation and AWE-PO show some oscillations, which will be investigated further. The wiggles inside the upstream results can also be found in [7].

Quantitatively, we compare the relative error of the acoustic intensity ε

$$\varepsilon_{\mathrm{LH/AWE-PO}} = \frac{\sum_i |I_{\mathrm{LH/AWE-PO}} - I_{\mathrm{DNS}}|_i}{\sum_i |I_{\mathrm{DNS}}|_i} \tag{7}$$

with respect to the DNS results, as reported in [7]. For Lighthill's equation, the relative error ε of the acoustic intensity is equal to 5.79% (maximum deviation of 1.7 dB) at the top arc and to 11.1% (maximum deviation of 2.2 dB) at the bottom arc compared to the DNS. For the AWE-PO results, the deviations are 6.75% (maximum deviation of 2.0 dB) at the top arc and 8.51% (maximum deviation of 1.75 dB) at the bottom arc compared to the DNS. Therefore, the errors of the acoustic intensity are in a comparable range to the errors presented in [44]. However, the line of extinction at about 12 degrees is visible remarkably well for the AWE-PO results. As mentioned in [7, Fig. 4], insufficient source domain integration and insufficient resolution of the source term of AWE-PO were tested and do not explain this extinction line. Neglecting the mean flow interaction with the fluctuating vortical flow inside the source of AWE-PO might be the reason for this extinction line. We will investigate this extinction effect in the future.
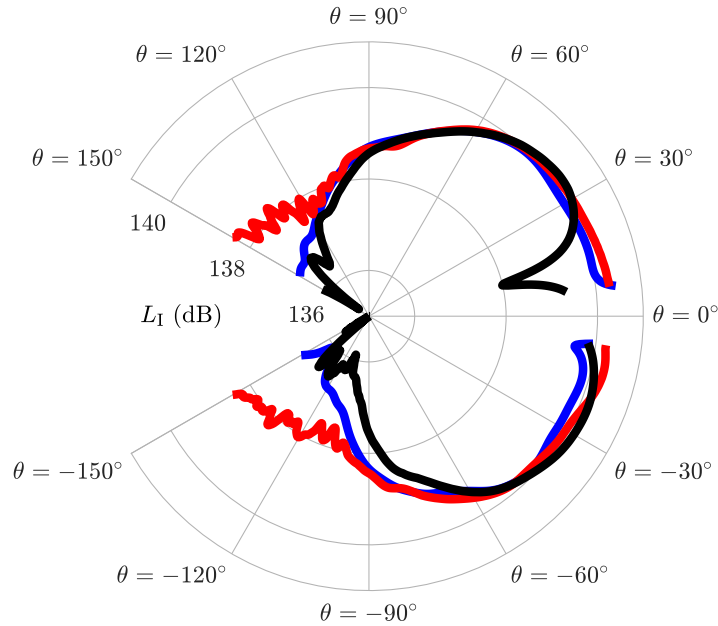
Fig. 8   Directivity of the acoustic intensity magnitude L_I depending on the angle θ, along a circle at the vortex pairing location $x/\delta_\omega = 110$ and $x/\delta_\omega = 0$ with a radius of $r/\delta_\omega = 140$. The results inside the mixing layer are excluded due to the high values inside the source region. Legend: — DNS, — Lighthill's equation, — AWE-PO.

VI. Conclusion

In [3] an acoustic wave equation based on Pierce's operator (AWE-PO) was introduced trough distinguishing between mean and fluctuating components. In doing so, sources of sound and convection effects are separated. This newly derived wave equation is applied to a two-dimensional mixing layer and the workflow can be applied in three steps. Firstly, a finite difference scheme obtains the DNS results. Based on this DNS result, the aeroacoustic sources are computed and applied to the acoustic wave equations, respectively. As the last step, the finite element method solves the wave propagation. The results of AWE-PO are compared with the pressure results of Lighthill's theory and the DNS.

The result section shows four visualizations of acoustic source terms: Lighthill's nonlinear source, the shear-noise part of Lighthill's source, the self-noise part of Lighthill's source, and the source of AWE-PO. Interestingly, Lighthill's nonlinear source contains the acoustic source but also the necessary convection and refraction effects to obtain a correct sound propagation. In contrast, the source term of AWE-PO has a much weaker magnitude and does not contain convective effects. Overall, Lighthill's equation and AWE-PO account reasonably well for acoustic propagation and convection effects. Finally, we would like to point out that a line of extinction occurs close to the mixing layer at 12 degree angle within the results obtained with AWE-PO. This might be due to the neglection of the mean flow interaction with the fluctuating vortical flow inside the AWE-PO source. Based on this ongoing study, the detailed effects of the shear-noise and self-noise contribution will be evaluated in the future to answer our hypothesis about the extinction line occurring in the results computed with AWE-PO.

A quantitative comparison of the direct numerical simulation results along an evaluation arc found an error of the acoustic intensity of less than 2 dB for Lighthill's equation and AWE-PO. This is comparable to the errors the reported for Lighthill's equation in other studies. This concludes that the presented wave equation AWE-PO reasonably predicts mixing layer sound, and that the acoustic far-field pressure results are in good agreement with the DNS.

Acknowledgements

of École Centrale de Lyon. It was performed within the framework of the LABEX CeLya (ANR-10-LABX-0060) of Université de Lyon, within the program *Investissements d'Avenir* (ANR-16-IDEX-0005) operated by the French National Research Agency (ANR).

Appendix - Explanation of the source term magnitude reduction of AWE-PO

The appendix describes the source magnitude reduction (of figure 2) of the AWE-PO mathematically and illustrates it by snapshots of the sources. As an outline, the individual source terms parts of the convective derivative are of the same order of magnitude and also of the same order of magnitude as the Lighthill source term. However, these two parts of the convective source term partly compensate for each other.
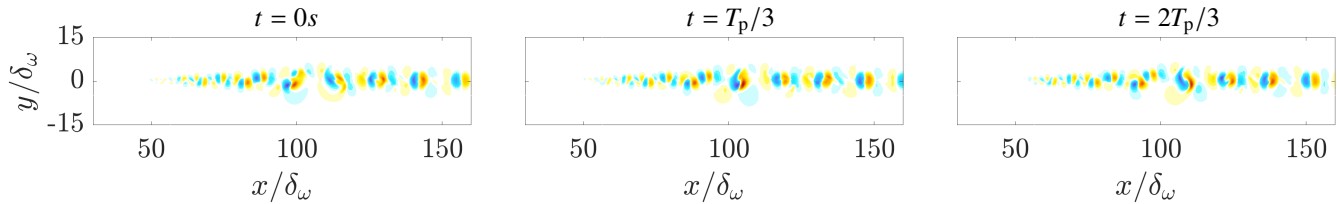

Fig. 9   Visualization of the partial time derivative part of the right-hand-side of AWE-PO (2)**, using a color scale minimum and maximum of** $\pm 3 \cdot 10^{10}$ kg/(m³s²)**, respectively. Comparability to the other source plots is achieved by including a relevant pre-factor** $1/(c_0^2 \Delta t)$ **to obtain the solution variable** p' **after solving AWE-PO for the scalar potential** ϕ**.**
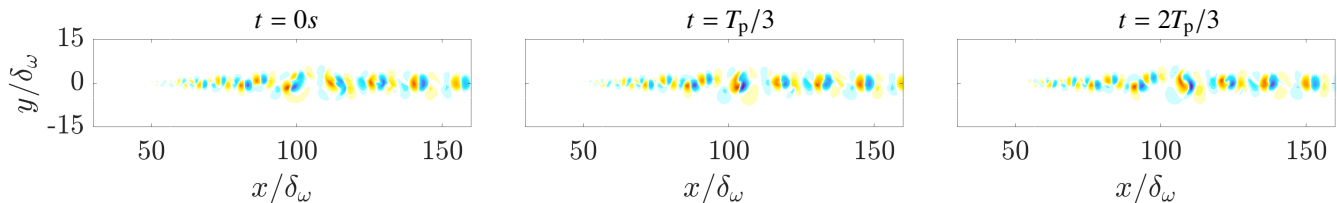

Fig. 10   Visualization of the convective derivative part of the right-hand-side of AWE-PO (2)**, using a color scale minimum and maximum of** $\pm 3 \cdot 10^{10}$ kg/(m³s²)**, respectively. Comparability to the other source plots is achieved by including a relevant pre-factor** $1/(c_0^2 \Delta t)$ **to obtain the solution variable** p' **after solving AWE-PO for the scalar potential** ϕ**.**

Fig. 11   Visualization of the right-hand-side of AWE-PO (2)**, using a color scale minimum and maximum of** $\pm 3 \cdot 10^{10}$ kg/(m³s²)**, respectively. Comparability to the other source plots is achieved by including a relevant pre-factor** $1/(c_0^2 \Delta t)$ **to obtain the solution variable** p' **after solving AWE-PO for the scalar potential** ϕ**.**
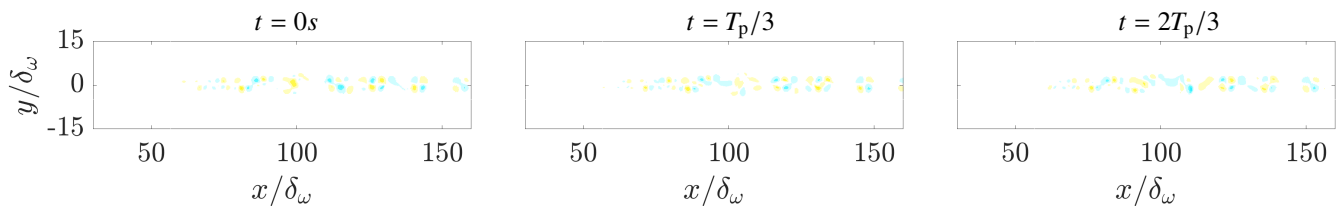
This strong reduction of the source magnitude is referred to as the filtering property of the convective derivative, which filters frozen flow structures S_m^f. Therefore, the individual source parts of AWE-PO are discussed to highlight the filtering property of the substantial derivative subject to frozen flow structures. Assume that the right-hand-side of the

AWE-PO is a source that can be arbitrary additively split into a frozen part $S_{\mathrm{m}}^{\mathrm{f}}$ and a remaining part S_{m}^{*}

$$S_{\mathrm{m}} = S_{\mathrm{m}}^{\mathrm{f}} + S_{\mathrm{m}}^{*}\,. \tag{8}$$

The frozen part will satisfy Taylor's Hypothesis and hence vanish

$$\frac{DS_{\mathrm{m}}^{\mathrm{f}}}{Dt} = 0\,. \tag{9}$$

Therefore and in the case of vortical structures, which are convected in a "nearly" frozen manner the source term S_{m} will be subject to a strong filtering and consequently reduction of the source magnitude.

By comparing the graphs of the sources figure 9 - 11 this strong magnitude reduction can be observed. Figure 9 shows the partial time derivative part of the right-hand-side of AWE-PO (2). This partial time derivative is mostly compensated by the convective derivative part of the right-hand-side of AWE-PO (2), illustrated in figure 9.

Overall, the right-hand side of AWE-PO (2) has a source amplitude reduction of one order of magnitude (see Fig. 11). Everything which remains in the source of AWE-PO are non-frozen source structures. Similar effects have been found in 3D for the perturbed convective wave equation and have not been explained yet [45, 46].

All sources removed by this substantial filtering technique in the source term of the AWE-PO do not radiate and are hence not efficiently converted into sound emission. Furthermore, the effect that a more anisotropically shaped self-noise source term is rearranged into a more isotropic source potential by the Laplace filter (3) is identified.

References

[1] Lighthill, M., "On sound generated aerodynamically I. General theory," *Proc. Roy. Soc. Lond.*, Vol. 211, No. A 211, 1952, pp. 564–587. https://doi.org/10.1098/rspa.1952.0060.

[2] Ribner, H., "The generation of sound by turbulent jets," *Advances in applied mechanics*, Vol. 8, Elsevier, 1964, pp. 103–182. https://doi.org/10.1016/S0065-2156(08)70354-5.

[3] Spieser, E., "Adjoint-based jet noise propagation model for the acoustic potential," Ph.D. thesis, École centrale de Lyon, Laboratoire de Mécanique des Fluides et d'Acoustique (LMFA) - CIFRE Safran Aircraft Engines, N° 2020LYSEC43, 2020. https://acoustique.ec-lyon.fr/publi/spieser_thesis.pdf.

[4] Spieser, É., and Bailly, C., "Sound propagation using an adjoint-based method," *Journal of Fluid Mechanics*, Vol. 900, 2020, p. A5. https://doi.org/10.1017/jfm.2020.469.

[5] Schoder, S., and Kaltenbacher, M., "Hybrid aeroacoustic computations: State of art and new achievements," *Journal of Theoretical and Computational Acoustics*, Vol. 27, No. 04, 2019, p. 1950020. https://doi.org/10.1142/S2591728519500208.

[6] Howe, M. S., *Theory of Vortex Sound*, Cambridge Texts in Applied Mathematics, 2003. https://doi.org/10.1017/CBO9780511755491.

[7] Margnat, F., and Gloerfelt, X., "On compressibility assumptions in aeroacoustic integrals: A numerical study with subsonic mixing layers," *The Journal of the Acoustical Society of America*, Vol. 135, No. 6, 2014, pp. 3252–3263. https://doi.org/10.1121/1.4875561.

[8] Fortuné, V., Lamballais, É., and Gervais, Y., "Noise radiated by a non-isothermal, temporal mixing layer. Part I: Direct computation and prediction using compressible DNS," *Theoretical and Computational Fluid Dynamics*, Vol. 18, No. 1, 2004, pp. 61–81. https://doi.org/10.1007/s00162-004-0114-8.

[9] Freund, J. B., "Noise sources in a low-Reynolds-number turbulent jet at Mach 0.9," *Journal of Fluid Mechanics*, Vol. 438, 2001, pp. 277–305. https://doi.org/10.1063/1.1569919.

[10] Pierce, A. D., "Wave equation for sound in fluids with unsteady inhomogeneous flow," *The Journal of the Acoustical Society of America*, Vol. 87, No. 6, 1990, pp. 2292–2299. https://doi.org/10.1121/1.399073.

[11] Bogey, C., and Bailly, C., "A family of low dispersive and low dissipative explicit schemes for flow and noise computations," *Journal of Computational Physics*, Vol. 194, No. 1, 2004, pp. 194–214. https://doi.org/10.1016/j.jcp.2003.09.003.

[12] Bogey, C., De Cacqueray, N., and Bailly, C., "A shock-capturing methodology based on adaptative spatial filtering for high-order non-linear computations," *Journal of Computational Physics*, Vol. 228, No. 5, 2009, pp. 1447–1465. https://doi.org/10.1016/j.jcp.2008.10.042.

[13] Berland, J., Bogey, C., Marsden, O., and Bailly, C., "High-order, low dispersive and low dissipative explicit schemes for multiple-scale and boundary problems," *Journal of Computational Physics*, Vol. 224, No. 2, 2007, pp. 637–662. https://doi.org/10.1016/j.jcp.2006.10.017.

[14] Tam, C. K., and Dong, Z., "Radiation and outflow boundary conditions for direct computation of acoustic and flow disturbances in a nonuniform mean flow," *Journal of Computational Acoustics*, Vol. 4, No. 02, 1996, pp. 175–201. https://doi.org/10.1142/S0218396X96000040.

[15] Bogey, C., and Bailly, C., "Three-dimensional non-reflective boundary conditions for acoustic simulations: far field formulation and validation test cases," *Acta Acustica united with Acustica*, Vol. 88, No. 4, 2002, pp. 463–471.

[16] Schoder, S., Roppert, K., Weitz, M., Junger, C., and Kaltenbacher, M., "Aeroacoustic source term computation based on radial basis functions," *International journal for numerical methods in engineering*, Vol. 121, No. 9, 2020, pp. 2051–2067. https://doi.org/10.1002/nme.6298.

[17] Schoder, S., Junger, C., Roppert, K., and Kaltenbacher, M., "Radial basis function interpolation for computational aeroacoustics," *AIAA AVIATION 2020 FORUM*, 2020 N. 2511. https://doi.org/10.2514/6.2020-2511.

[18] Schoder, S., Wurzinger, A., Junger, C., Weitz, M., Freidhager, C., Roppert, K., and Kaltenbacher, M., "Application limits of conservative source interpolation methods using a low Mach number hybrid aeroacoustic workflow," *Journal of Theoretical and Computational Acoustics*, Vol. 29, No. 1, 2050032, 2021. https://doi.org/10.1142/S2591728520500322.

[19] Schoder, S., Junger, C., Weitz, M., and Kaltenbacher, M., "Conservative source term interpolation for hybrid aeroacoustic computations," *25th AIAA/CEAS aeroacoustics conference*, 2019 N. 2538. https://doi.org/10.2514/6.2019-2538.

[20] Li, Y., Tanahashi, M., and Miyauchi, T., "Sound generation in compressible mixing layers," *JSME International Journal Series B Fluids and Thermal Engineering*, Vol. 44, No. 4, 2001, pp. 505–512. https://doi.org/10.1299/jsmeb.44.505.

[21] Bogey, C., Bailly, C., and Juvé, D., "Numerical simulation of sound generated by vortex pairing in a mixing layer," *AIAA Journal*, Vol. 38, No. 12, 2000, pp. 2210–2218. https://doi.org/10.2514/2.906.

[22] Kaltenbacher, M., Roppert, K., Schoder, S., Freidhager, C., Mayrhofer, D., Toth, F., Junger, C., and Floss, S., "opencfs.org," , 2020.

[23] Schoder, S., "Aeroacoustic analogies based on compressible flow data," Ph.D. thesis, TU Wien, 2019.

[24] Schoder, S., Roppert, K., and Kaltenbacher, M., "Helmholtz's decomposition for compressible flows and its application to computational aeroacoustics," *SN Partial Differential Equations and Applications*, Vol. 1, No. 6, 2020, pp. 1–20. https://doi.org/10.1007/s42985-020-00044-w.

[25] Schoder, S., Roppert, K., and Kaltenbacher, M., "Postprocessing of Direct Aeroacoustic Simulations Using Helmholtz Decomposition," *AIAA Journal*, Vol. 58, No. 7, 2020, pp. 3019–3027. https://doi.org/10.2514/1.J058836.

[26] Schoder, S., Toth, F., Freidhager, C., and Kaltenbacher, M., "Revisiting infinite mapping layer for open domain problems," *Journal of Computational Physics*, Vol. 392, 2019, pp. 354–367. https://doi.org/10.1016/j.jcp.2019.04.067.

[27] Kaltenbacher, B., Kaltenbacher, M., and Sim, I., "A modified and stable version of a perfectly matched layer technique for the 3-d second order wave equation in time domain with an application to aeroacoustics," *Journal of Computational Physics*, Vol. 235, 2013, pp. 407–422. https://doi.org/10.1016/j.jcp.2012.10.016.

[28] Kaltenbacher, M., Roppert, K., Schoder, S., and Heinz, J., "Stable Finite Element Formulation for the Perturbed Convective Wave Equation," *EuroNoise 2021*, 2021, p. 8.

[29] Bogey, C., Bailly, C., and Juvé, D., "Computation of flow noise using source terms in linearized Euler's equations," *AIAA Journal*, Vol. 40, No. 2, 2002, pp. 235–243. https://doi.org/10.2514/6.2000-2047.

[30] Bogey, C., Gloerfelt, X., and Bailly, C., "Illustration of the inclusion of sound-flow interactions in Lighthill's equation," *AIAA Journal*, Vol. 41, No. 8, 2003, pp. 1604–1606. https://doi.org/10.2514/2.2115.

[31] Samanta, A., Freund, J. B., Wei, M., and Lele, S. K., "Robustness of Acoustic Analogies for Predicting Mixing-Layer Noise," *AIAA Journal*, Vol. 44, No. 11, 2006, pp. 2780–2786. https://doi.org/10.2514/1.22186.

[32] Nana, C., Marx, D., Prax, C., and Fortuné, V., "Hybrid aeroacoustic computation of a low Mach number non-isothermal shear layer," *Computers & Fluids*, Vol. 93, 2014, pp. 30–40. https://doi.org/10.1016/j.compfluid.2014.01.006.

[33] Cheung, L. C., and Lele, S. K., "Linear and nonlinear processes in two-dimensional mixing layer dynamics and sound radiation," *Journal of Fluid Mechanics*, Vol. 625, 2009, pp. 321–351. https://doi.org/10.1017/S0022112008005715.

[34] Hiraishi, M., Tsutahara, M., and Leung, R., "Numerical simulation of sound generation in a mixing layer by the finite difference lattice Boltzmann method," *Computers & Mathematics with Applications*, Vol. 59, No. 7, 2010, pp. 2403–2410. https://doi.org/10.1016/j.camwa.2009.08.073.

[35] Zhou, L., Wan, Z., Sun, D.-J., and Wei, M., "Sound generation by different vortex interactions in mixing layers," *50th AIAA Aerospace Sciences Meeting including the New Horizons Forum and Aerospace Exposition*, 2012, p. 1173. https://doi.org/10.2514/6.2012-1173.

[36] Golanski, F., Moser, C., Nadal, L., Prax, C., and Lamballais, E., "Numerical methodology for the computation of the sound generated by a non-isothermal mixing layer at low Mach number," *Direct and Large-Eddy Simulation VI*, Springer, 2006, pp. 529–536. https://doi.org/10.1007/978-1-4020-5152-2_61.

[37] Moser, C., Lamballais, E., and Gervais, Y., "Direct computation of the sound generated by isothermal and non-isothermal mixing layers," *12th AIAA/CEAS Aeroacoustics Conference (27th AIAA Aeroacoustics Conference)*, 2006, p. 2447. https://doi.org/10.2514/6.2006-2447.

[38] Colonius, T., Lele, S. K., and Moin, P., "Sound generation in a mixing layer," *Journal of Fluid Mechanics*, Vol. 330, 1997, pp. 375–409. https://doi.org/10.1017/S0022112096003928.

[39] Monkewitz, P. A., and Huerre, P., "Influence of the velocity ratio on the spatial instability of mixing layers," *The Physics of Fluids*, Vol. 25, No. 7, 1982, pp. 1137–1143. https://doi.org/10.1063/1.863880.

[40] Bogey, C., "Calcul direct du bruit aérodynamique et validation de modeles acoustiques hybrides," Ph.D. thesis, Ecully, Ecole Centrale de Lyon, 2000.

[41] Powell, A., "Theory of Vortex Sound," *J. Acoust. Soc. Am.*, Vol. 36, 1964, pp. 177 – 196. https://doi.org/doi.org/10.1121/1.1918931.

[42] Phillips, O. M., "On the generation of sound by supersonic turbulent shear layers," *J. Fluid Mech.*, Vol. 9, 1960, pp. 1–18. https://doi.org/10.1017/S0022112060000888.

[43] Lilley, G. M., "On the noise from jets," Tech. rep., AGARD CP-131, 1974.

[44] Moser, C., Lamballais, E., Margnat, F., Fortuné, V., and Gervais, Y., "Numerical study of Mach number and thermal effects on sound radiation by a mixing layer," *International Journal of Aeroacoustics*, Vol. 11, No. 5-6, 2012, pp. 555–579. https://doi.org/10.1260/1475-472X.11.5-6.555.

[45] Schoder, S., Maurerlehner, P., Wurzinger, A., Hauser, A., Falk, S., Kniesburges, S., Döllinger, M., and Kaltenbacher, M., "Aeroacoustic sound source characterization of the human voice production-perturbed convective wave equation," *Applied Sciences*, Vol. 11, No. 6, 2021, p. 2614. https://doi.org/10.3390/app11062614.

[46] Schoder, S., Junger, C., and Kaltenbacher, M., "Computational aeroacoustics of the EAA benchmark case of an axial fan," *Acta Acustica*, Vol. 4, No. 5, 2020, p. 22. https://doi.org/10.1051/aacus/2020021.